Chemosphere 254 (2020) 126829

Contents lists available at ScienceDirect

Chemosphere

journal homepage: www.elsevier.com/locate/chemosphere

Superior removal of inorganic and organic arsenic pollutants from water with MIL-88A(Fe) decorated on cotton fibers

Da Pang [a], Chong-Chen Wang [a, *], Peng Wang [a], Wen Liu [b], Huifen Fu [a], Chen Zhao [a]

[a] Beijing Key Laboratory of Functional Materials for Building Structure and Environment Remediation, Beijing University of Civil Engineering and Architecture, Beijing, 100044, China
[b] The Key Laboratory of Water and Sediment Sciences, Ministry of Education, College of Environment Sciences and Engineering, Peking University, Beijing, 100871, China

HIGHLIGHTS

- **MIL-88A(Fe)** exhibits excellent adsorption abilities toward different arsenics.
- **MIL-88A(Fe)** decorated on cotton fibers maintains outstanding adsorption activities.
- The combination of **MIL-88A(Fe)** and cotton fibers improves its stability.
- **MIL-88A(Fe)** decorated on cotton fibers achieves good reusability.
- **MIL-88A(Fe)** decorated on cotton fibers exhibits potential large-scale application.

GRAPHICAL ABSTRACT

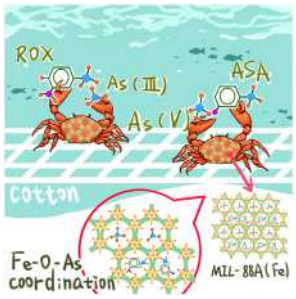

ARTICLE INFO

Article history:
Received 16 February 2020
Received in revised form
14 April 2020
Accepted 16 April 2020
Available online 21 April 2020

Handling Editor: Y Yeomin Yoon

Keywords:
MIL-88A(Fe)
Cotton fibers
Organic arsenics
Inorganic arsenics
Adsorptive removal

ABSTRACT

Arsenic contamination has attracted worldwide concerns, owing to its toxicity and severe threat to human and environment. It is urgent to develop efficient adsorbents to remove arsenic pollutants. Within this paper, both pristine **MIL-88A(Fe)** and **MIL-88A(Fe)** decorated on cotton fibers were successfully fabricated using an eco-friendly method. The pristine **MIL-88A(Fe)** displayed outstanding adsorption performances towards four selected arsenic pollutants, in which the adsorption capacities toward As(III), As(V), ROX and ASA were 126.5, 164.0, 261.4 and 427.5 mg g^{-1}, respectively. Additionally, **MIL-88A(Fe)** exhibited excellent removal efficiencies in a wide pH range and with the presence of different co-existing ions. It was proposed that the coordinative interactions of As—O—Fe between arsenic pollutants and **MIL-88A(Fe)** contributed to the superior adsorption performances. Furthermore, two **MIL-88A(Fe)**/cotton fibers composites were synthesized by both post synthesis (**MC-1**) and in-situ synthesis (**MC-2**), which demonstrated identically outstanding adsorption activities toward four selected arsenic pollutants. **MC-1** and **MC-2** enhanced the stability and reusability of **MIL-88A(Fe)**, which was challenging issues of pristine **MIL-88A(Fe)** powder. Additionally, the fixed-bed column packed by **MC-1** or **MC-2** can continuously eliminate arsenic pollutants from the water flow. This work provided a new possibility of metal-organic frameworks to accomplish potentially large-scale application to purify the arsenic-contaminated water.

* Corresponding author.
E-mail address: chongchenwang@126.com (C.-C. Wang).

https://doi.org/10.1016/j.chemosphere.2020.126829
0045-6535/

1. Introduction

Among toxic elements, arsenic (As) is one of the most hazardous contaminants in water environment, as it is originated from natural sources like soils, rocks along with volcanic activity, and anthropogenic sources like wood preservatives, pesticides, pharmaceuticals, pigment industries (Hughes et al., 2011). The long-term and chronical exposure to arsenic contaminated water can lead to diarrhea, muscle weakness, neurological disorder, irregular heartbeat, impairments of the immune system, cancers, and even death in extreme cases (Hughes et al., 2011; Moghimi et al., 2015; Song et al., 2017). Hence, the maximum permissible arsenic level in drinking water has been set as 10 μg L^{-1} by the Environmental Protection Agency (EPA) and World Health Organization (WHO) (Smith et al., 2002). Generally, the arsenic mainly exists as inorganic forms of As(V), As(III) and organic compounds like arsanilic acid (ASA, $C_6H_8AsNO_3$), roxarsone (ROX, $C_6H_6AsNO_6$) in water environment. Inorganic As(III) are highly toxic, which is approximate 60 times more poisonous than inorganic As(V) (Smedley and Kinniburgh, 2002). Organic arsenic like ASA and ROX are widely used as feed additives in the pork and poultry industries, which can be emitted into water and soil (Sierra-Alvarez et al., 2010; Wang and Cheng, 2015), which can eventually be converted into highly toxic inorganic As(III) and As(V) compounds (Jun et al., 2015). Therefore, the removal of both inorganic and organic arsenic is highly significant and desirable (Wang et al., 2019). So far, many techniques like oxidation, precipitation, coagulation, co-precipitation, sorption, membrane have been adopted to achieve arsenic removal (Ahmad et al., 2020; Choong et al., 2007; Guan et al., 2012; Zhang et al., 2019). Adsorption is regarded as a promising technique due to its low cost, simple operation, no need of expensive reagents and catalysts as well as proceeding at ambient operation temperature/pressure (Jung et al., 2015). Adsorption technology is desirable due to simple operation and low cost, which is strongly dependent on adsorbents. Traditional adsorbents including activated carbon (Chen et al., 2007), metal oxides (Joshi et al., 2017), and polymers (Poon et al., 2014) have been investigated, which are facing some problems like low adsorption capacity, and slow adsorption rate. It is still important and challenging to explore efficient and eco-friendly adsorbents for the superior decontamination of arsenic in water.

Metal-organic frameworks (MOFs), three-dimension frameworks built up of metal templates and organic linkers, are unique types of highly porous crystalline materials (Cai et al., 2016; Wang et al., 2014). Benefiting from the controlled porosity, ultra-high specific surface areas, structural tailorability, MOFs have been extensively investigated in catalysis and photocatalysis (Wang et al., 2019; Yi et al., 2019), adsorption toward organic and heavy metal pollutants (Du et al., 2017; Xu et al., 2018), energy gas storage (Farha et al., 2010), sensing (Song et al., 2018; Wang et al., 2019), and so on (Liu et al., 2018). Recently, many MOFs like UiO-66, UiO-67-NH_2, and MIL-100(Fe) were utilized to accomplish removal of arsenic from wastewater (He et al., 2019; Jun et al., 2015; Tian et al., 2018). Some outstanding achievements in the field of arsenic removal using MOFs as adsorbents were accomplished. Nowadays, Fe-based MOFs like MIL-53(Fe), MIL-88A(Fe), MIL-88B(Fe), MIL-100(Fe) and MIL-101(Fe) are attracted increasing attentions because of the non-toxicity, low cost and biocompatibility of Fe template, easy availability of the organic linkers, as well as the excellent physicochemical features (Hou et al., 2018). Due to remarkable water and chemical stability, easy formation of Fe−O−As coordination interaction between Fe-MOF and arsenic pollutants, Fe-based MOFs have been widely applied for arsenic adsorption (Jun et al., 2015; Vu et al., 2015). **MIL-88A(Fe)**, consisting of oxo-centered trimers of iron(III) octahedrals connected by fumarate linkers, possessed 3D framework with interconnected pores and cages, which exhibited ultrahigh adsorption capacity towards NO (McKinlay et al., 2013) and n-Alkanes (Ramsahye et al., 2013). However, according to previous researches, most synthetic methods of **MIL-88A(Fe)** suffered from using hazardous organic solvents and adopting time-consuming hydrothermal conditions (Liao et al., 2019), which limited its wide application. Our research group developed an eco-friendly and high throughput synthetic method to easily produce **MIL-88A(Fe)** under room temperature (Fu et al., 2019), which provided possibility to accomplish low-cost adsorptive removal various arsenic pollutants with **MIL-88A(Fe)**. However, it was hard to accomplish continuous adsorptive removal due to the possible adsorbent loss with the flow of solution (Li et al., 2020). Within this work, the water stable **MIL-88A(Fe)**, a Fe-based metal-organic framework, was grown on cotton fibers via both post synthetic method and in-situ growth method. The **MIL-88A(Fe)** decorated on cotton fibers displayed superior adsorption abilities toward inorganic As(III), inorganic As(V), ASA and ROX in batch and continuous experiments, in which the adsorption kinetics, thermodynamics, influence factors and mechanism was investigated. This work provided a new possibility to clean pollutants from water with adsorbents loaded on substrates like natural cottons.

2. Experimental

The used chemicals and reagents along with the corresponding characterization instruments were listed in Electronic Supplementary Information (ESI).

2.1. Synthesis of MIL-88A(Fe)

MIL-88A(Fe) was prepared by using an eco-friendly method (Fu et al., 2020), which was described in ESI.

2.2. Fabrication of MIL-88A(Fe)/Cotton

2.2.1. Post synthetic method

1.0 g pure cotton fabric and 1.0 g as-prepared **MIL-88A(Fe)** powder were mixed into 150 mL of deionized water, which was agitated by magnetic stirrer for 8 h with a speed of 850 rpm at room temperature. The obtained **MIL-88A(Fe)**/Cotton (**MC-1**) was washed with deionized water and ethanol (99%) several times to remove the weakly bonded **MIL-88A(Fe)**, and dried at 333 K until the complete evaporation of water and ethanol, which can guarantee the uniformity of the as-prepared **MIL-88A(Fe)**/cotton fibers composites. The parallel fabrication experiments were carried out for 10 times to ensure the controlled amount of MIL-88A(Fe) being coated onto cotton fibers, in which the relative errors of loaded amounts of **MIL-88A(Fe)** onto cotton fibers is within ±5% (Table S1).

2.2.2. In-situ growth method

The procedure for in-situ growth of **MIL-88A(Fe)**/Cotton (**MC-2**) was similar to the synthesis of pristine **MIL-88A(Fe)** (Section 2.1), expect that 1.0 g pure cotton fabric was added to the aqueous solution containing 1.0 mmol $FeCl_3 \cdot 6H_2O$ (2.7029 g) and 1.0 mmol fumaric acid (1.1607 g). The obtained **MC-2** was washed by deionized water and ethanol (99%) several times to remove the unbounded **MIL-88A(Fe)**, and dried at 333 K until the complete evaporation of molecular water and ethanol. The parallel fabrication experiments were carried out for 10 times, which was identical to that of the **MIL-88A(Fe)**/Cotton (**MC-1**).

2.3. Adsorption experiments

The adsorption kinetic studies were performed at pH = 5 for

ROX, at pH = 11 for ASA, As(III) and As(V) with the initial inorganic arsenic solution concentration from 1 to 50 mg L^{-1} along with the initial organic arsenic solution concentration from 1 to 150 mg L^{-1}, while the dosages of the pristine **MIL-88A(Fe)** as adsorbent were kept at 0.2 g L^{-1}. To obtain the adsorption isotherms and thermodynamic parameters, the corresponding experiments were conducted under 298 K, 303 K and 308 K at a speed of 170 rpm for 48 h.

The experiments towards simulate different treated water samples (the details are listed in Table S2) were performed by adding 0.4 g **MIL-88A(Fe)**, 0.54 g **MC-1** or **MC-2** to 200 mL inorganic and organic arsenic solution. During the adsorption process, every 4.0 mL samples were drawn with springe filter (0.22 μm) from the mixtures. The residual inorganic and organic arsenic concentrations were determined by ICP-OES (ICP-5000, Focused Photonics Inc., China) with the detection limit being 5.5 μg L^{-1}.

2.4. Fixed-bed column experiments

The fixed-bed column experiments were performed to investigate the potential large-scale application, in which 1.08 g **MC-1** or 1.08 g **MC-2** was packed in a glass column with length of 340 mm and diameter of 16 mm. As illustrated in Fig. 12a, the flow rate in term of the superficial liquid velocities (SLV) is maintained as 6.0 mL min^{-1} by a constant flow longer precision pump. The bed depth, bed volume, empty bed contact time (EBCT) and hydraulic loading rate are listed in Table S3. The simulated wastewater samples containing organic arsenics (like ROX and ASA) with concentration of 1.0 mg L^{-1} and inorganic arsenics (like As(III) and As(V)) with concentration of 0.5 mg L^{-1} were pumped through the column from top to bottom. The residual inorganic and organic arsenic concentrations in the effluent were measured by ICP-OES with the detection limit being 5.5 μg L^{-1}.

2.5. Data analysis

The adsorption kinetic were analyzed by the pseudo-first-order and pseudo-second-order kinetic models, Langmuir isotherms, Freundlich and Dubinin–Radushkevich adsorption models were applied to fit the adsorption isotherms. Thermodynamic parameters were obtained by previous reported method. Details of the methods are described in the Supporting information.

3. Results and discussion

3.1. Characterization

The peaks at 7.6°, 10.2°, 13.0°, 14.1°, 15.2° and 20.9° in the powder X-ray diffraction (PXRD) patterns (Fig. S1) of the as-prepared **MIL-88A(Fe)** matched well with those of the previously reported **MIL-88A(Fe)** (Liu et al., 2018; Xu et al., 2014), implying that **MIL-88A(Fe)** could be synthesized adopting our reported method. In the PXRD patterns of **MC-1** and **MC-2**, the peaks at 14.7°, 16.6° and 22.8° were ascribed to the cotton fibers, while the characteristic peaks of **MIL-88A(Fe)** couldn't be observed due to the tiny content of **MIL-88A(Fe)** in the **MC-1** and **MC-2** samples (Fig. S1) (Abdelhameed et al., 2018). Possibly, the strong diffraction peaks of cotton fibers could overlap the relatively weak diffraction peaks of **MIL-88A(Fe)**, which was similar to the UiO-66-NH_2 decorated on Al_2O_3 substrate (Du et al., 2019).

Moreover, the FTIR spectra of the as-prepared **MIL-88A(Fe)**, **MC-1** and **MC-2** samples were depicted in Fig. S2. As to the as-prepared pristine **MIL-88A(Fe)**, the broad absorption band appearing around 3300–3500 cm^{-1} were ascribed to the O–H stretching vibrations of the water molecules(Gholizadeh Khasevani and Gholami, 2018). The two intense peaks at 1396 cm^{-1} and 1603 cm^{-1} were assigned to the symmetric and asymmetric vibration modes of the carboxyl group, respectively, indicating that the dicarboxylate linkers were presented in the **MIL-88A(Fe)** framework (Gholizadeh Khasevani and Gholami, 2018; Liu et al., 2018). The peaks at 560 cm^{-1} was ascribed to the Fe–O vibration of **MIL-88A(Fe)** (Lv et al., 2015). As to the cotton fibers, the peak at 1642 cm^{-1}, 2890 cm^{-1} and 3327 cm^{-1} were contributed to the stretching vibration of C=C, $-CH_3$ and –OH group, respectively (Gargoubi et al., 2016; Lv et al., 2014). These absorption peaks were corresponding to the structure of cellulose in cotton fibers. The characteristic peaks at 560 cm^{-1}, 1396 cm^{-1} and 1603 cm^{-1} in both **MC-1** and **MC-2** were originated from **MIL-88A(Fe)** decorated on the cotton fibers, affirming the successful fabrication of **MIL-88A(Fe)**/cotton. It is noteworthy noting that a new peak at 1724 cm^{-1} in **MIL-88A(Fe)**/cotton is attributable to COOH group and COOR group (not carboxylate). These peaks suggest that esterification reaction took place between the carboxyl group of **MIL-88A(Fe)** and the hydroxyl group of cotton surface (Fiamingo and Campana-Filho, 2016; Xu et al., 2017).

The morphology and particle size of as-prepared **MIL-88A(Fe)** were investigated by SEM and TEM images. As illustrated in Fig. 1, the pristine **MIL-88A(Fe)** displayed uniform and well-crystallized hexagonal micro-rods with an average size of 700–1200 nm in length and 200–400 nm in diameter, which was slightly smaller than those in the previous reports (Huang et al., 2018; Liu et al., 2018; Xu et al., 2014). As to **MC-1**, **MIL-88A(Fe)** particles were uniformly distributed over cotton fibers (Fig. 2a and b and Fig. S3a). While, as to **MC-2**, the **MIL-88A(Fe)** particles were distributed densely (Fig. 2d and Fig. S3b) or sparsely (Fig. 2e) over partial locations of the cotton fibers. The successful decoration of **MIL-88A(Fe)** on cotton fibers was further affirmed by the elemental mapping (Fig. 2c and f).

To determine the surface composition and chemical states of **MC-1** and **MC-2**, the X-ray photoelectron spectrum (XPS) analysis was conducted. As displayed in Fig. 3a, the characteristic peaks of C, O and Fe were observed in the XPS spectra of **MC-1** and **MC-2**. As found in Fig. 3b, the C 1 s spectrum was divided into four peaks at binding energy of 288.54, 287.02, 286.00 and 284.38 eV in **MC-1** and 288.51, 287.29, 286.02 and 284.41 eV in **MC-2**. The carboxylate groups and C–C of the completely deprotonation of fumarate were corresponded to the peaks with binding energies at 288.54/288.51 eV and 284.38/284.41 eV, respectively (Huang et al., 2018; Liao et al., 2019; Liu et al., 2018). The peaks with binding energy of 286.00/286.02 eV, 287.02/287.29 eV and 288.54/288.51 eV in **MC-1** and **MC-2** could be ascribed to C=O, C–OH and C–O–C of cotton fibers and ester groups (Xu et al., 2017; Yang et al., 2009). Fig. 3c displayed the high-resolution XPS spectra of O 1s, which could be split into five peaks at binding energies of 533.54/533.32 eV, 532.98/532.93 eV, 532.34/532.49 eV, 531.69/531.86 eV and 530.51(530.91) eV, attributing to the O–H of the surface hydroxyl groups, the C–O and O–C=O bond of cotton fabric and ester groups, oxygen components on the carboxylate groups of the fumarate and the Fe–O bonds of the **MC-1**/**MC-2**, respectively (Ding et al., 2018; Liao et al., 2019; Liu et al., 2018). These results further affirmed that **MIL-88A(Fe)** have been covalently linked on cotton surface via formation of ester groups (Naebe et al., 2016). As shown in Fig. 3d, the high-resolution XPS spectrum of Fe 2p could be divided into the Fe $2p_{3/2}$ (711.2/711.28 eV) and Fe $2p_{1/2}$ (725.01/725.05 eV) with a satellite signal at 715.66/715.27) eV for **MC-1** and **MC-2**. The peak distance between the Fe $2p_{3/2}$ and the Fe $2p_{1/2}$ was approximately 13.8 eV, which was well coincide with previous references for Fe_2O_3, and it was important characteristic of Fe(III) existed in **MC-1** and **MC-2** (Li et al., 2017; Yu et al., 2011). Furthermore, the binding energy of Fe 2p doublet for **MC-1** and **MC-2** displayed the mild shift of binding energy to the lower energy in comparison with the Fe(III) typical peaks of the **MIL-88A(Fe)**

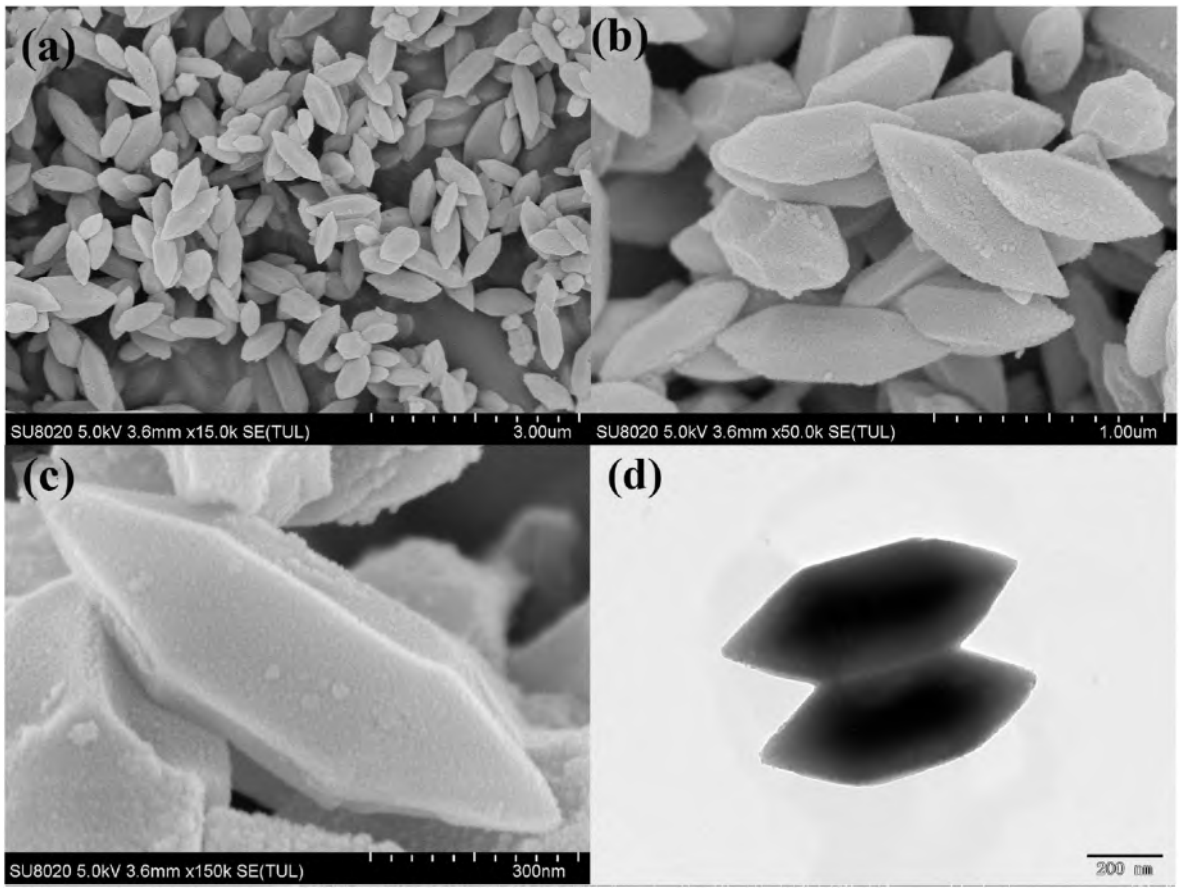

Fig. 1. (a, b, c) SEM and (d) TEM image of pristine **MIL-88A(Fe)**.

(Fig. 6d), which can be ascribed to the compact interfacial contact between **MIL-88A(Fe)** and cotton fibers in the **MC-1** and **MC-2** (Liang et al., 2015a,b; Xia et al., 2019). According to previously reported papers (Muñiz et al., 2009; Xia et al., 2019), the presence of Fe(III) species facilitated to oxidize more poisonous As(III) into lower toxicity As(V), which was favorable to be adsorbed onto the surface of adsorbents. The loaded **MIL-88A(Fe)** was slightly high for post synthetic composite (ca. 80.0 mg g^{-1}) and exceeded the amounts loaded onto the in-situ composite (ca. 60.0 mg g^{-1}). In all, the XPS determination along with FTIR, PXRD, SEM and TEM confirmed the successful decoration of **MIL-88A(Fe)** onto cotton fibers.

3.2. Adsorption kinetics

The adsorption rate is a key factor for efficiently treating As-contaminated water (You et al., 2020; Yu et al., 2019). To gain an insight into the adsorption kinetics behaviors of **MIL-88A(Fe)**, the time-dependence of inorganic and organic arsenic removal with various initial concentrations were given in Fig. S4, Fig. S6, Fig. S8 and Fig. S10. For the initial As(III) concentrations of 1 and 5 mg L^{-1}, when the equilibrium was reached, the As(III) removal efficiency reached 98.12 and 95.60% within 120 min, respectively. For the initial ROX, ASA, As(V) concentrations of 1, 5 and 10 mg L^{-1}, the adsorption equilibrium can be rapidly reached within 30 min, and the residual arsenic concentration could be declined to below 10 μg L^{-1}. Considering that the concentrations of organic and inorganic arsenics in the water environment even in contaminated water body were always low (generally no more than 2.5 mg L^{-1}), the adsorption behaviors of **MIL-88A(Fe)** indicated that it was an outstanding and potential adsorbent for highly effective arsenic capture in the practical application. The corresponding fitted kinetic parameters were listed in Table S4, Table S7, Table S10 and Table S13. All the sorption kinetic curves were more fitted in the pseudo-second-order model with the outstanding correlation coefficients (R^2 > 0.995) and the theoretical adsorption capacities calculated from the pseudo-second-order kinetic model were in good agreement with the experimental values (Table S4, Table S7, Table S10 and Table S13). The results demonstrated that the rate-controlling step might be chemisorption, and the adsorption capacity were determined by the number of active sites (B. Liu et al., 2015).

3.3. Adsorption isotherms

In order to determine the maximum adsorption capacity and adsorption isotherms behaviors of **MIL-88A(Fe)**, the adsorption isotherm studies were conducted. The adsorption isotherms behaviors of **MIL-88A(Fe)** at different temperatures like 298, 303 and 308 K toward different organic and inorganic arsenic with different initial concentrations were presented in Fig. S5, Fig. S7, Fig. S9 and Fig. S11, respectively. The maximum adsorption capacity of pristine **MIL-88A(Fe)** towards As(III), As(V), ROX and ASA was 126.5, 164.0, 261.4 and 427.5 mg g^{-1}, respectively, which was higher than those of counterpart adsorbents listed in Table 1. Although some adsorbents like the UiO-66, UiO-67 and ZIF-8 (Wang et al., 2019) could achieve higher adsorption capacity toward selected arsenic pollutants than **MIL-88A(Fe)**, it was worthy noting that the as-

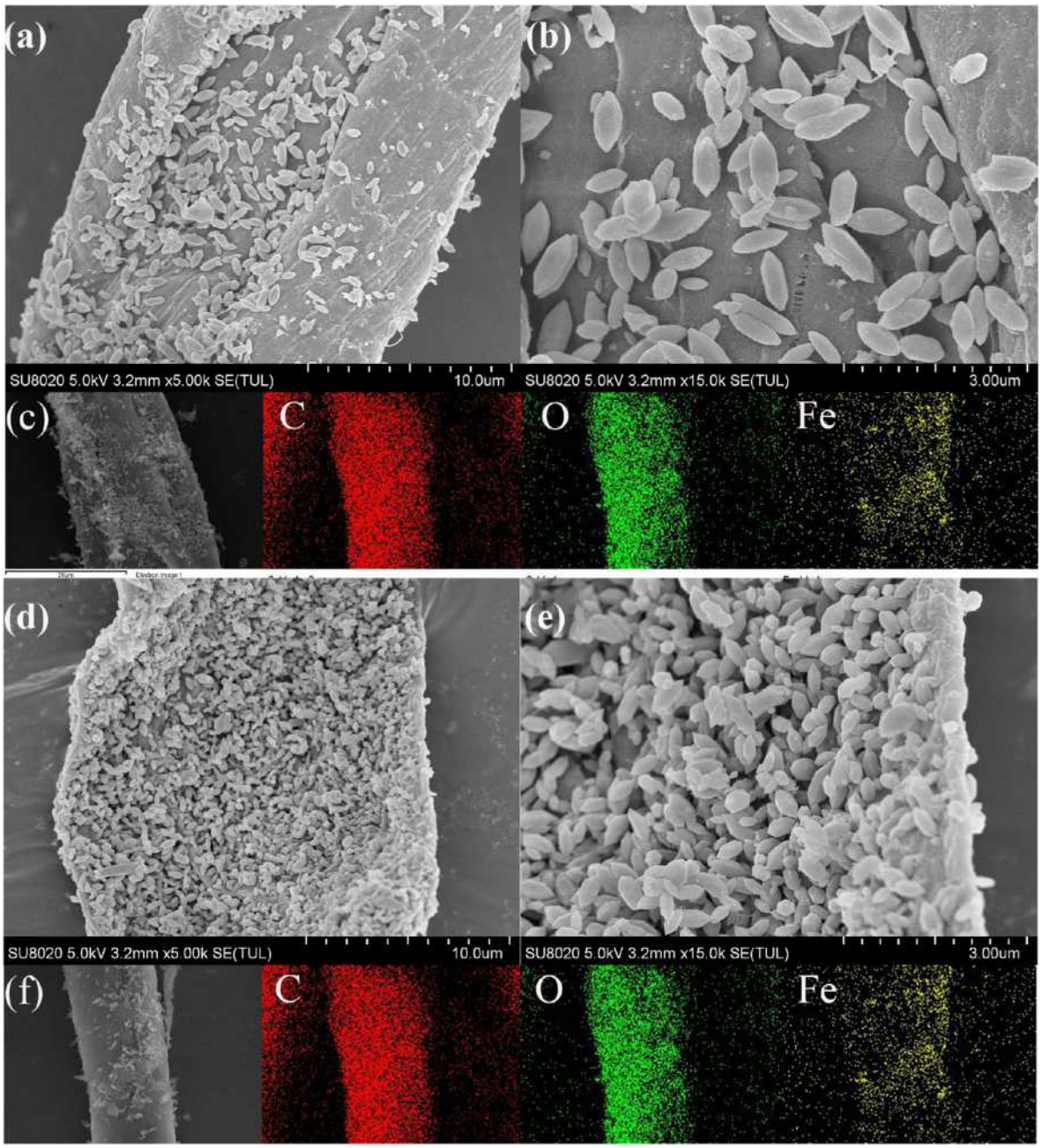

Fig. 2. SEM image of (a, b) **MC-1** and (d, e) **MC-2**; Elemental mappings of (c) **MC-1** and (f) **MC-2**.

prepared **MIL-88A(Fe)** displayed superior adsorption performance toward different arsenic pollutants like not only inorganic arsenic pollutants but also organic arsenic pollutants with low concentration. For example, mesoporous ZIF-8 possessed the higher maximum adsorption capacity (791 mg g^{-1}) toward ASA than the as-prepared **MIL-88A(Fe)** in this study, but the adsorption capacity of **MIL-88A(Fe)** ($q_{e0.03} \approx 50$ mg g^{-1}) was higher than that of mesoporous ZIF-8 ($q_{e0.03} = 0.76$ mg g^{-1}) toward ASA with equilibrium concentration of 30 μg L^{-1} (Jung et al., 2015). With the good adsorption performance toward different organic and inorganic arsenics, **MIL-88A(Fe)** could be potentially applied in the treatment of natural wastewater with low contents of arsenic pollutants.

To get further insight into the adsorption isotherms behaviors of **MIL-88A(Fe)**, the adsorption isotherm models, and thermodynamic parameters were studied. As shown in Table S5, Table S8, Table S11 and Table S14, the higher correlation coefficient values and the maximum adsorption capacities calculated from Langmuir plots indicated these adsorption isotherms were well followed the Langmuir model (Wang et al., 2020). All the calculated thermodynamic parameters including the standard free energy ΔG°, enthalpy ΔH° and entropy ΔS° were illustrated in Table S6, Table S9, Table S12 and Table S15, respectively. The negative values of all ΔG° implied that the adsorption process was spontaneous in the nature. The negative value of ΔH° was observed for the adsorptive interaction between **MIL-88A(Fe)** and ROX indicated the endothermic nature of sorption process, while the positive value of ΔH° for the interactions between **MIL-88A(Fe)** and As(III)/As(V)/ASA revealed that the corresponding processes were exothermic. The positive

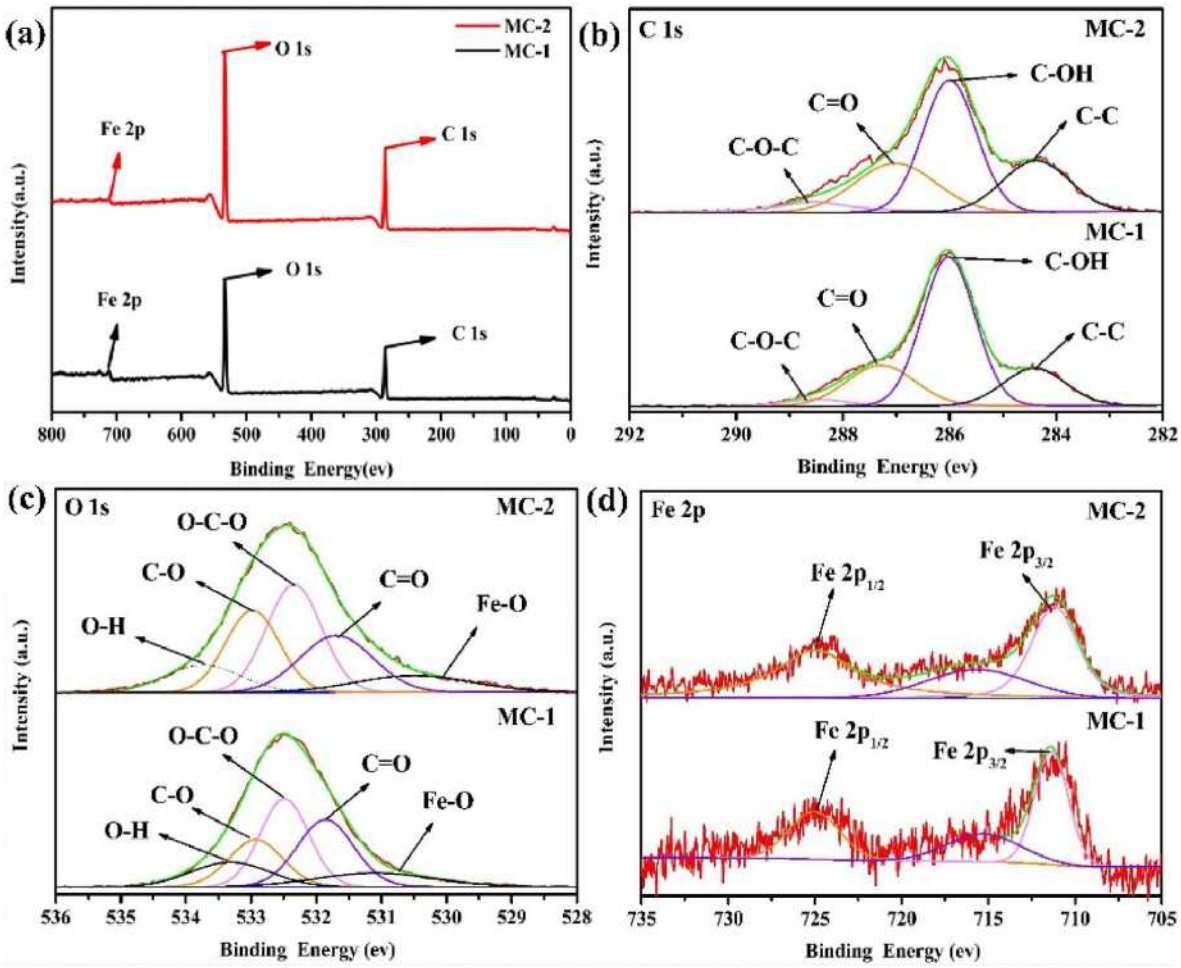

Fig. 3. XPS spectrums of **MC-1** and **MC-2**: (a) survey spectrum, (b) C 1s, (c) O 1s, and (d) Fe 2p.

Table 1
Comparison of **MIL-88A(Fe)** with various adsorbents for arsenic removal (298 K).

Arsenic species	Adsorbents	Adsorption capacity (mg g^{-1})	pH	Refs.
As(V)	MIL-53(Fe)	21.3	5	Vu et al. (2015)
As(V)	$Cell_{MW}$-HPEI fibers	99.3	4	Deng et al. (2016)
As(V)	Hierarchical ZIF-8	90.9	N/A	Wu et al. (2014)
As(V)	MIL-100(Fe)	110.0	7	Cai et al. (2016)
As(V)	NH_2-MIL-88(Fe)	125.0	6	Xie et al. (2017)
As(V)	MIL-88B(Fe)	156.7	6	Hou et al. (2018)
As(V)	$MnFe_2O_4$ Magnetic Nanoparticles	68.3	2.1	Hu et al. (2017)
As(V)	Fe_3O_4@MIL101(Cr)	80.0	7	Folens et al. (2016)
As(V)	MIL-88A(Fe)	164.0	11	This work
As(III)	CuO nanoparticles	26.9	8	Martinson and Reddy (2009)
As(III)	Fe_3O_4@ZIF-8	100.0	8	Huo et al. (2018)
As(III)	Fe_3O_4@MIL101(Cr)	121.5	7	Folens et al. (2016)
As(III)	2D ZIF-L	43.7	10	Nasir et al. (2018)
As(III)	MIL-88A(Fe)	126.5	11	This work
ASA	$MnFe_2O_4$ Magnetic Nanoparticles	59.5	2.1	Hu et al. (2017)
ASA	UiO-67-NH_2	178.0	4	Tian et al. (2018)
ASA	MIL-101$(OH)_3$	238.0	4	Sarker et al. (2017)
ASA	MIL-100(Fe)	366.0	4	(Jun et al., 2015)
ASA	NH_2-MIL-68(In)	401.6	5	Lv et al. (2018)
ASA	MIL-88A(Fe)	427.5	11	This work
ROX	$MnFe_2O_4$ Magnetic Nanoparticles	51.5	2.1	Hu et al. (2017)
ROX	CNT/C@Fe/chitosan	142.9	6	Ma et al. (2015)
ROX	MIL-100(Fe)	387.0	N/A	(Jun et al., 2015)
ROX	MIL-88A(Fe)	261.4	5	This work

value of ΔS° suggested the increased of randomness during the adsorption process of **MIL-88A(Fe)** toward different selected arsenic targets (Hu et al., 2017). These results demonstrated that the adsorption of **MIL-88A(Fe)** toward ROX was a spontaneous, endothermic and the random process, while the adsorptive interactions of **MIL-88A(Fe)** toward As(III), As(V) and ASA were spontaneous, exothermic and the random processes.

3.4. Effect of pH

The pH value of arsenic solution have a great effect on adsorption characteristics, because it determines surface properties of adsorbents along with the anionic species of arsenic (Nasir et al., 2018). The zeta potentials of as-prepared pristine **MIL-88A(Fe)** in the pH range of 4.0–12.0 were displayed in Fig. S12, in which it decreased with the increase of pH, and the isoelectric point (IEP) value was ca. 7.0. The adsorption performances of **MIL-88A(Fe)** towards different organic and inorganic arsenics in the pH range from 2.0 to 12.0 were illustrated in Fig. 4. As to ROX and As(V), efficient removal (nearly 100%) was accomplished at wide pH range from 3.0 to 11.0, and the optimum pH values for ROX and As(V) removal were 5.0 and 11.0, respectively. For ASA, the optimum removal efficiency with maximum value of 94.7% occurred at pH = 11.0, and the removal efficiency of ASA was still maintained over 75% in the pH range of 5.0–10.0. The As(III) removal efficiencies were extremely low under the acidic and weak alkalinous conditions (pH ranging from 2.0 to 8.0), and increased rapidly with the increasing pH from 8.0 to 11.0. **MIL-88A(Fe)** exhibited optimum removal efficiency with 92.6% at pH = 11.0. As well known, the pK_a values of ROX are 3.43, 6.38 and 9.67, and the pK_a values of ASA are 1.9, 4.1 and 9.2, indicating both organic arsenics presented as anionic species ($C_6H_4AsNO_6^{2-}$ and $C_6H_3AsNO_6^{3-}$ for ROX, as well as $C_6H_6AsO_3^{2-}$ and $C_6H_5AsO_3^{3-}$ for ASA) under the conditions of pH > 7.0 (Li et al., 2016; Tian et al., 2018). Meanwhile, the inorganic As(V) displayed anionic species as $HAsO_4^{2-}$ and AsO_4^{3-} as pH > 7.0, and inorganic As(III) demonstrated H_2AsO^{3-}, $HAsO_4^{2-}$ and AsO_4^{3-} at pH above 9.2 (Chen et al., 2013; K. Liu et al., 2015). These findings suggested that electrostatic interaction was not a vital factor controlling the adsorption process of **MIL-88A(Fe)** toward different organic and inorganic arsenic pollutants (Song et al., 2018). It could be observed that **MIL-88A(Fe)** displayed outstanding adsorption performances toward ROX and As(V) in wide pH range, implying that it could be used as potential adsorbent to achieve uptake toward arsenic pollutants from real water environment without adjusting pH condition. And, if the pH values of the treated water samples were controlled in the suitable range, **MIL-88A(Fe)** also accomplish satisfied As(III) and ASA removal.

3.5. Effect of co-existing ions

As typical trace contaminants, the concentrations of different arsenics in common water environment were reported to be below 2.5 mg L^{-1} and even below 0.5 mg L^{-1} in most cases (Choong et al., 2007; X. Liu et al., 2015). To test the influences from co-existing ions, tap water, lake water and rain water were adopted to simulate different treated water samples containing selected inorganic arsenics (the concentration of As(III) and As(V): 0.5 mg L^{-1}) and organic arsenics (ROX and ASA: 1 mg L^{-1}). As illustrated in Fig. 5, the ASA, ROX, As(V) and As(III) concentration decreases dramatically with the addition of **MIL-88A(Fe)**, in which the nearly 100% removal efficiencies could be accomplished within 20, 20, 5, 90 min, respectively. It was worthy to noting that the residual ASA,

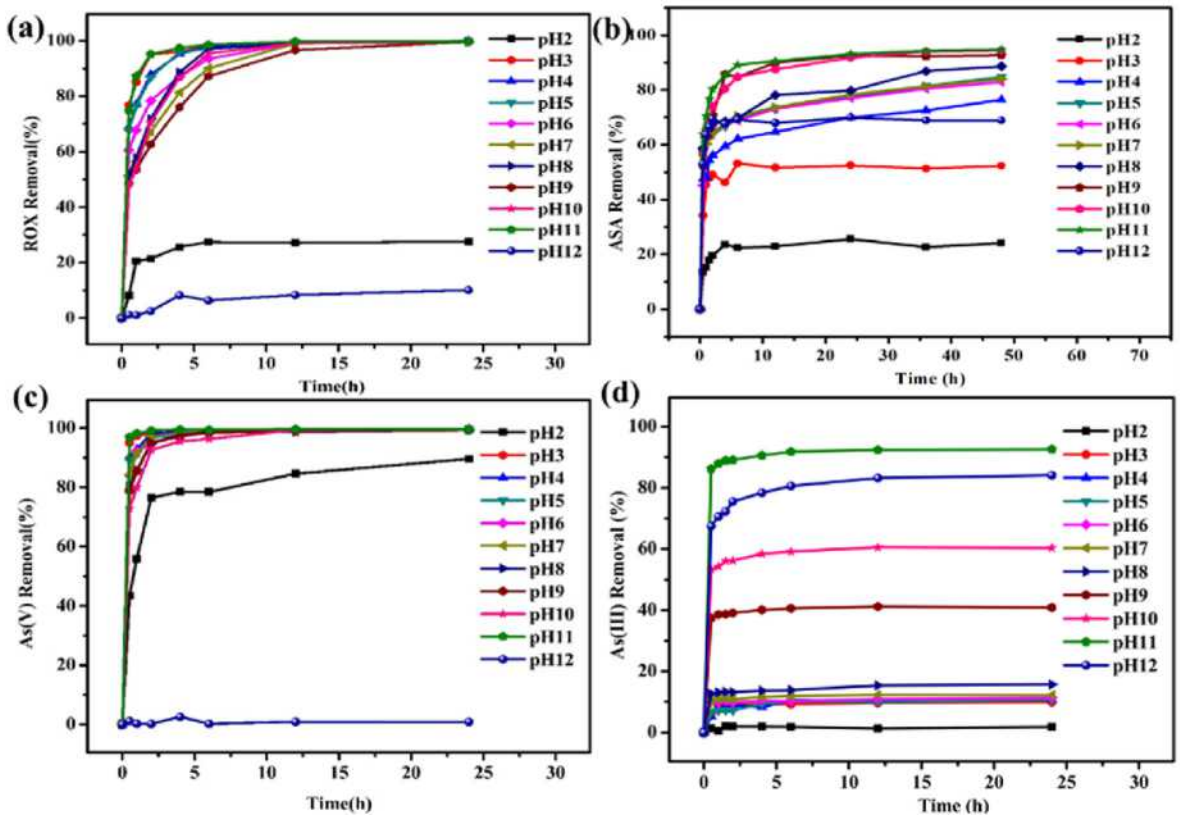

Fig. 4. The adsorption capacity of **MIL-88A(Fe)** toward (a) ROX, (b) ASA, (c) As(V), and (d) As(III) under various pH values (Initial ROX and ASA concentration: 25 mg L^{-1}; Initial As(V) and As(III) concentration: 10 mg L^{-1}).

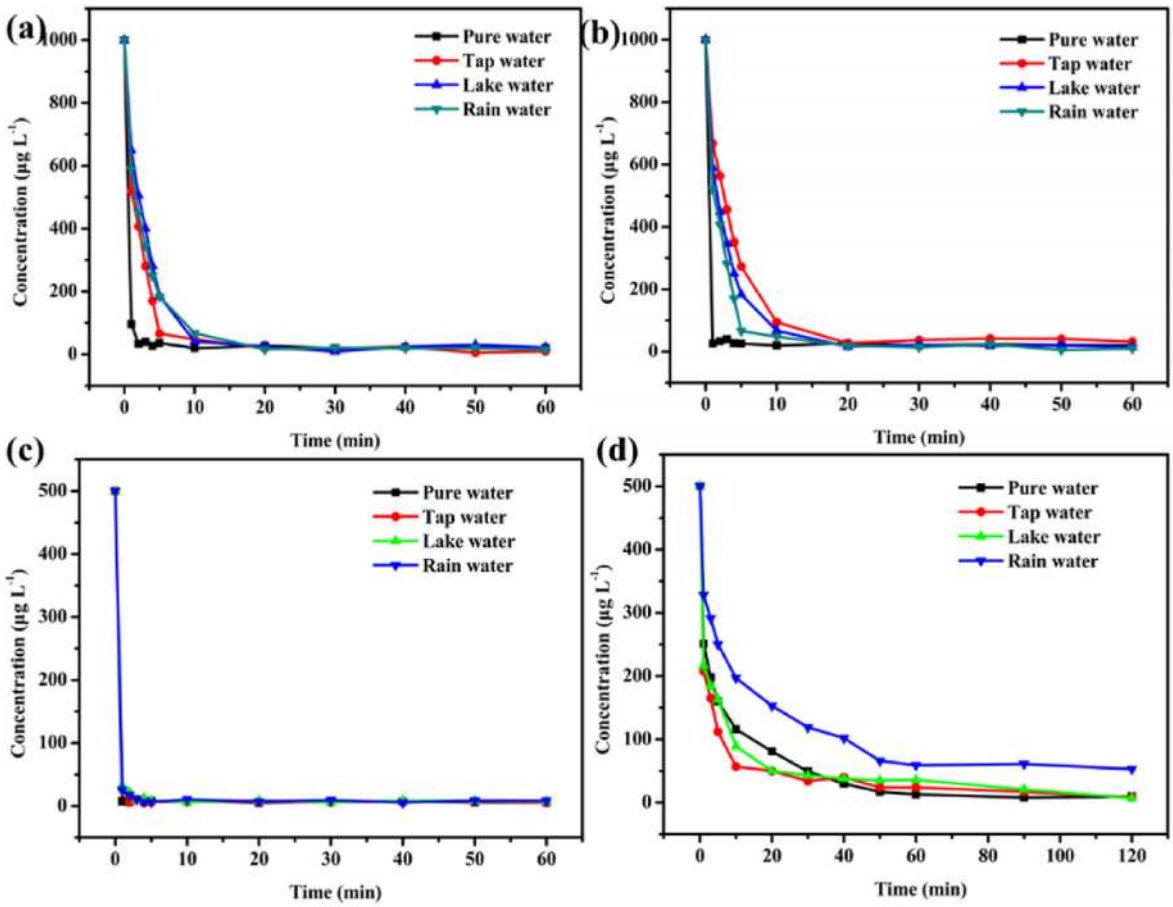

Fig. 5. The adsorption of (a) ASA, (b) ROX, (c) As(V), and (d) As(III) made up by pure, tap, lake, and rain water on the obtained **MIL-88A(Fe)** (Initial ASA and ROX concentration: 1.0 mg L^{-1}; Initial As(v) and As(III) concentration: 0.5 mg L^{-1}).

ROX, As(V) and As(III) concentrations after being adsorbed by **MIL-88A(Fe)** were lower than those required by drinking water standards, WHO (10 μg L^{-1} for As(V), As(III), 29 μg L^{-1} for ROX and 35 μg L^{-1} for ASA) (Choong et al., 2007; Wang et al., 2019). It is noteworthy that the dissolved organic matter (DOM) can strongly interact with inorganic and organic contaminants to affect their transformation, transportation and toxicity (Zhao et al., 2018). In this study, the results revealed that DOM didn't exert remarkable influence the adsorptive performances of **MIL-88A(Fe)** towards arsenic contaminants, which was comparable to the adsorptive performances of UiO-67 towards organic arsenic (Tian et al., 2018). Both high removal efficiency and fast equilibrium time suggested that the **MIL-88A(Fe)** was a highly efficient adsorbent for removing inorganic and organic arsenic pollutants from real water environment.

3.6. Possible adsorption mechanism

Previous researches had verified that the surface area was a significant factor for the adsorption performance (Li et al., 2016). But in this study, the BET surface area of pristine **MIL-88A(Fe)** is 13.29 m^2 g^{-1}, implying that its outstanding adsorption performance towards inorganic and organic arsenic might not be assigned to its porous structure (Xiao et al., 2015). The zeta potentials of **MIL-88A(Fe)** ranged from 1.8 to −6.9 mV at pH being 4.0–12.0, demonstrating that the strong affinity with different arsenic species might not be attributed to electrostatic interaction (Sarker et al., 2017). To further elucidate the interaction between various arsenic pollutants and pristine **MIL-88**, the elemental mappings, FTIR and XPS spectra of **MIL-88A(Fe)** were obtained before and after arsenic adsorption. The elemental mapping obtained from SEM verified that the presence of arsenic in **MIL-88A(Fe)** after adsorbing different arsenics (Fig. 6). The immobilization of arsenic on the surface of **MIL-88A(Fe)** can be also confirmed by XPS determination (Fig. S13). After adsorbing arsenic, a new binding energy peak appeared at ca. 45.3 eV, which can be ascribed to As 3d peak. Two new peaks with weak intensity at 828 cm^{-1} and 733 cm^{-1} appeared in the FTIR spectra of **MIL-88A(Fe)** adsorbing arsenic adsorption, which corresponded to the protonated As–O–H bond of the adsorbed arsenate and As–O bond in the As–O–Fe linkage (Lv et al., 2015; Sui et al., 2016). The above-stated characterizations confirmed the interactions between arsenics and **MIL-88A(Fe)**.

To further determine the strong affinity between arsenic and **MIL-88A(Fe)**, the high-resolution XPS determinations of O1s in **MIL-88A(Fe)** before and after arsenic adsorption were conducted. Prior to adsorption, O1s spectra in the pristine **MIL-88A(Fe)** could be divided into three peaks at 533.5, 531.9 and 530.5 eV (Fig. 7b), corresponding to the surface hydroxyl groups, the oxygen components of the carboxyl groups and the Fe–O bonds in **MIL-88A(Fe)** (Liang et al., 2015a,b; Xie et al., 2017). After the adsorption toward ROX, a new O 1s peak appeared at 531.34 eV, which could be ascribed to As–O (Kang et al., 2013). The results matched well with the corresponding FTIR spectra analysis. Similar XPS analyses for

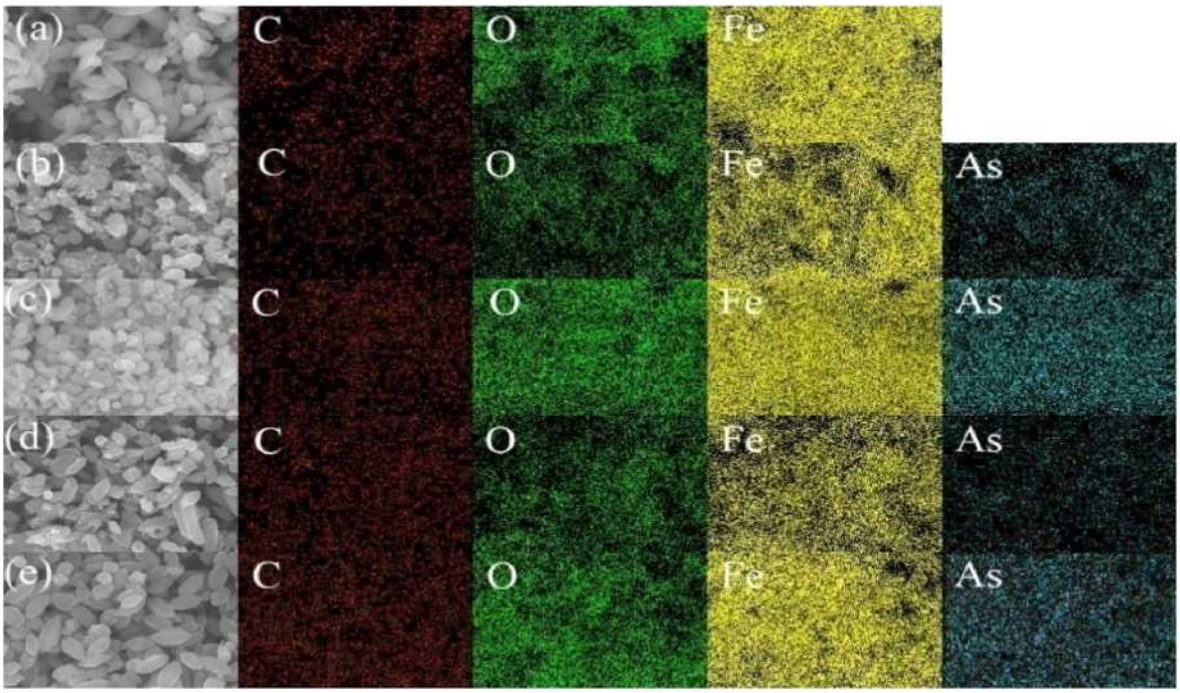

Fig. 6. (a) Elemental mapping of **MIL-88A(Fe)** before adsorption, (b) after As(V) adsorption, (c) after As(III) adsorption, (d) after ASA adsorption, and (e) after ROX adsorption.

adsorptive interaction between **MIL-88A(Fe)** and As(III)/As(V)/ASA were performed, and the corresponding XPS and FTIR spectra were illustrated in Fig. S13 and Fig. S14. It was observed that the binding energy of Fe 2p displayed mild deviation to higher energy (Fig. 7c), which can be assigned to the strong interaction between As in ROX and Fe3-μ3-oxo clusters in **MIL-88A(Fe)** (Hou et al., 2018; Xie et al., 2017). These results indicated that the adsorption of **MIL-88A(Fe)** toward different arsenic pollutants resulted from the formation of As—O—Fe linkages, which was consistent with the pseudo-second-order adsorption kinetics modeling (Hou et al., 2018) (see Fig. 8). Furthermore, FTIR, XRD (Fig. S15) and SEM (Fig. S16 and Fig. S17) revealed that the morphology and crystalline structure of **MIL-88A(Fe)** were well maintained after the interaction with different arsenic species, implying good stability of **MIL-88A(Fe)** during the adsorption process in water surrounding (Jian et al., 2015).

3.7. The adsorption performances of MC-1 and MC-2

It was well known that it was difficult to achieve recovery and separation of the powder adsorbents(Valizadeh et al., 2018). Our experiment result illustrated in Fig. 11a confirmed that powder **MIL-88A(Fe)** was hard to be separated from the treated water samples for reuse, as the powder **MIL-88A(Fe)** was declined to be suspended in the water solution. To solve the awkward situation faced by the powder adsorbents, it was expected to fabricate the adsorbents on some substrates (Du et al., 2019; Li et al., 2019). One of our strategies is to decorate **MIL-88A(Fe)** on the cottons fibers via both post synthetic method and in-situ growth method. To eliminate possible interference, the controlled experiments were conducted and the results revealed that blank cotton displayed nearly no adsorption activities towards different arsenic species. As depicted in Fig. 9 and Fig. 10, **MC-1** and **MC-2** exhibited outstanding adsorption activities toward four selected arsenic pollutants in different water samples simulated by pure water, tap water, lake water and rain water. The adsorption rates over **MC-1** and **MC-2** toward different arsenic pollutants were slower than those of pristine **MIL-88A(Fe)** (Figs. 9 and 10). As demonstrated in Fig. 11d, the leaking of Iron (Fe) from **MC-1** and **MC-2** ranged from 0.015 mg L^{-1} to 0.033 mg L^{-1} during the adsorption process, which were much lower than the pristine **MIL-88A(Fe)**. Furthermore, the residual arsenic solution after adsorptive treatment using **MC-1** and **MC-2** were clear (Fig. 11b and c), which exhibited good recovery and separation superior to **MIL-88A(Fe)** powder (Fig. 11a). The results demonstrated that **MIL-88A(Fe)**/cotton fibers exhibited excellent removal efficiency and fast equilibrium rate towards different arsenic pollutants. Due to ultrahigh adsorption capacity, **MIL-88A(Fe)**/cotton fiber composites can be used for many times in simulated nature water until reaching adsorptive saturation. Furthermore, **MIL-88A(Fe)** was hard to be separated from the surface of cotton fibers during adsorption process and nearly no substance leaked to the water environment. The cotton fibers can be processed into thread and further be weaved into mesh, which can be put into treated water to capture arsenic pollutants and be pulled from the water after adsorptive saturation.

3.8. Fixed bed column experiments

The continuous adsorptive removal toward pollutants in fixed-bed column is always desired in large-scale operation due to that it is easy to operate and offers us many useful parameters during pollutants removal (Wang et al., 2015). In this study, the column was packed by **MIL-88A(Fe)**/cotton fibers rather than the individual **MIL-88A(Fe)** particles to avoid the loss of packed adsorbent particles and to guarantee the rapid flow of targeted solution. The fixed bed column was adopted to remove the inorganic and organic arsenic pollutants from continuous flow of simulated wastewater (Fig. 12a), in which the concentrations of As(V), As(III), ROX and ASA were 0.5, 0.5, 1.0 and 1.0 mg L^{-1}, respectively. It was found that the effective treatment volume of **MC-1** toward ROX was 288 BVs (2.88 L) (Fig. 12b), in which the maximum permissible

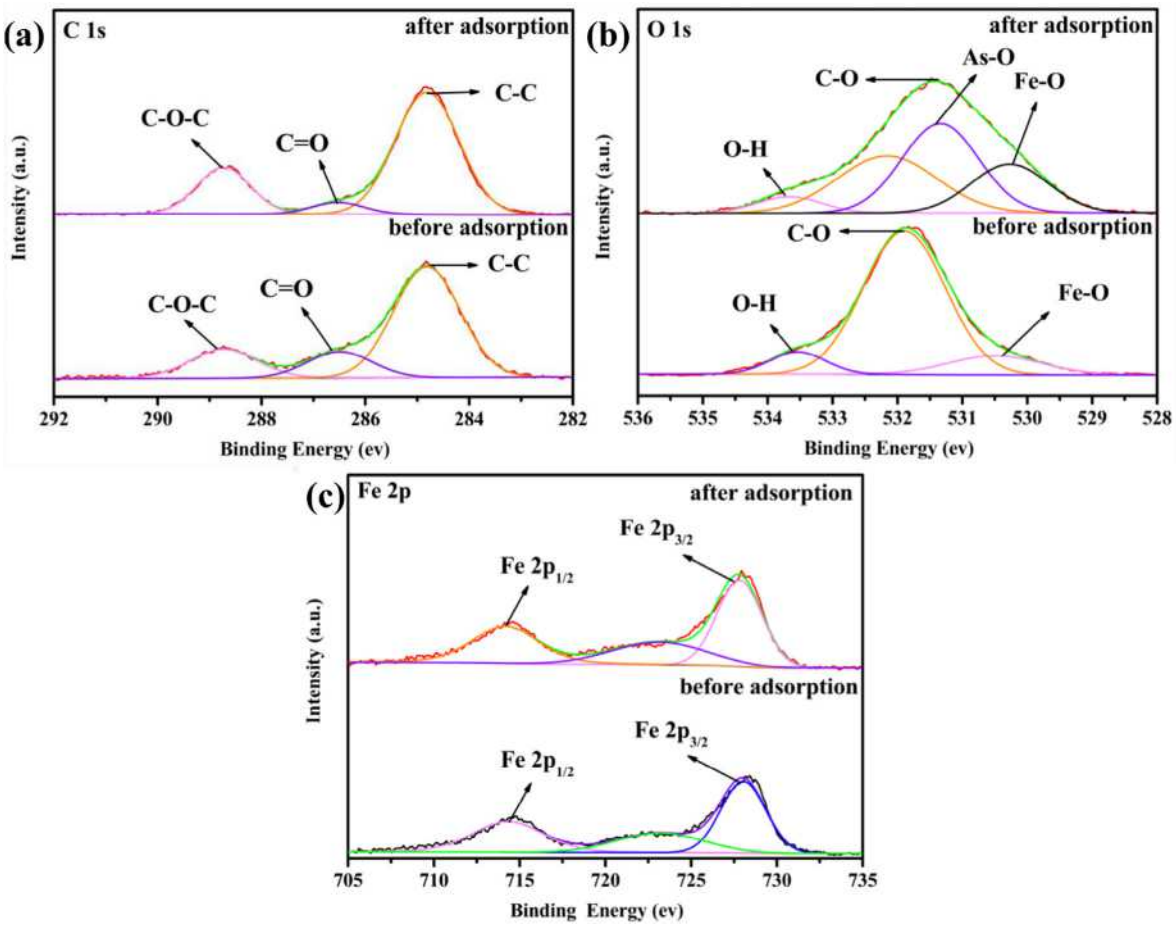

Fig. 7. (a) XPS spectra of C 1s, (b) XPS spectra of O 1s, and (c) XPS spectra of Fe 2p before and after arsenic adsorption (only ROX was shown as an example).

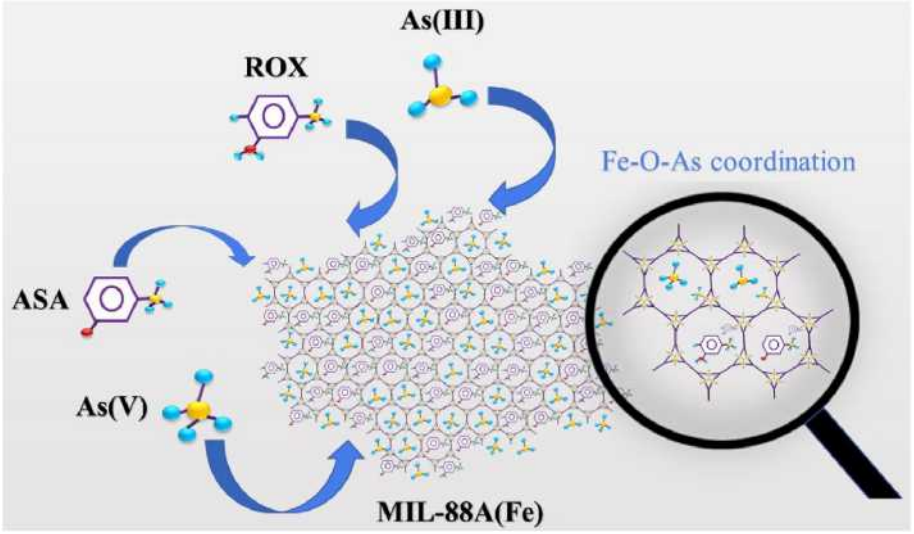

Fig. 8. Proposed interaction mechanism between **MIL-88A(Fe)** and four different arsenic pollutants.

concentration of ROX (29 μg L^{-1}) and removal efficiency of 98.14% were achieved. The adsorption capacity of the **MC-1** fixed bed was nearly exhausted up to 3000 BVs (30 L) of continuous inflow of ROX solution (ca. 80 h). The effective treatment volume and the exhaustion volume were subject to the adsorbent loading mass (Zietzschmann et al., 2016). As the outcomes of breakthrough curves were demonstrated in Fig. S18 and Fig. S19, the effective treatment volumes of **MC-1** and **MC-2** toward ASA, ROX and As(V)

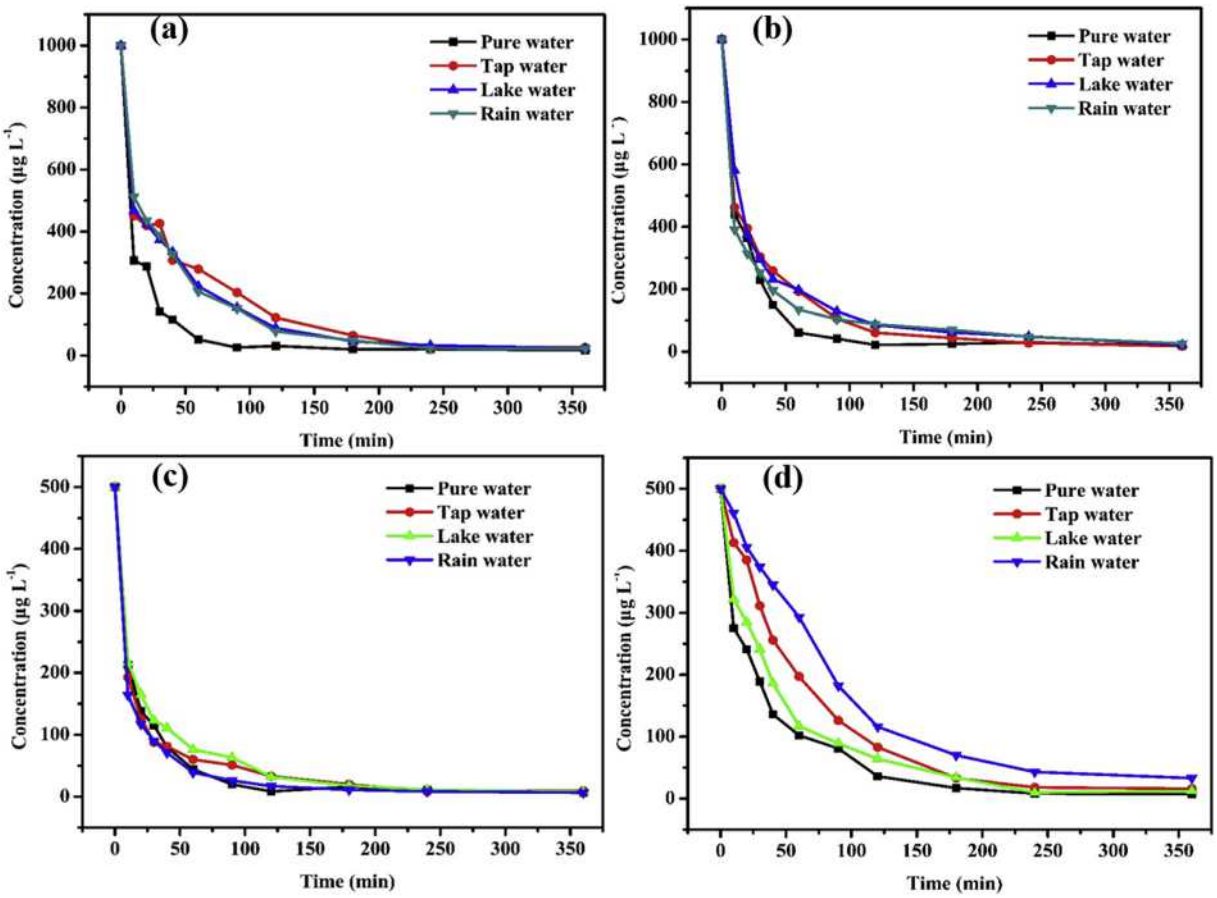

Fig. 9. The adsorption of (a) ASA, (b) ROX, (c) As(V), and (d) As(III) made up by pure, tap, lake, and rain water on the obtained **MC-1** (Initial ASA and ROX concentration: 1 mg L^{-1}; Initial As(v) and As(III) concentration: 0.5 mg L^{-1}).

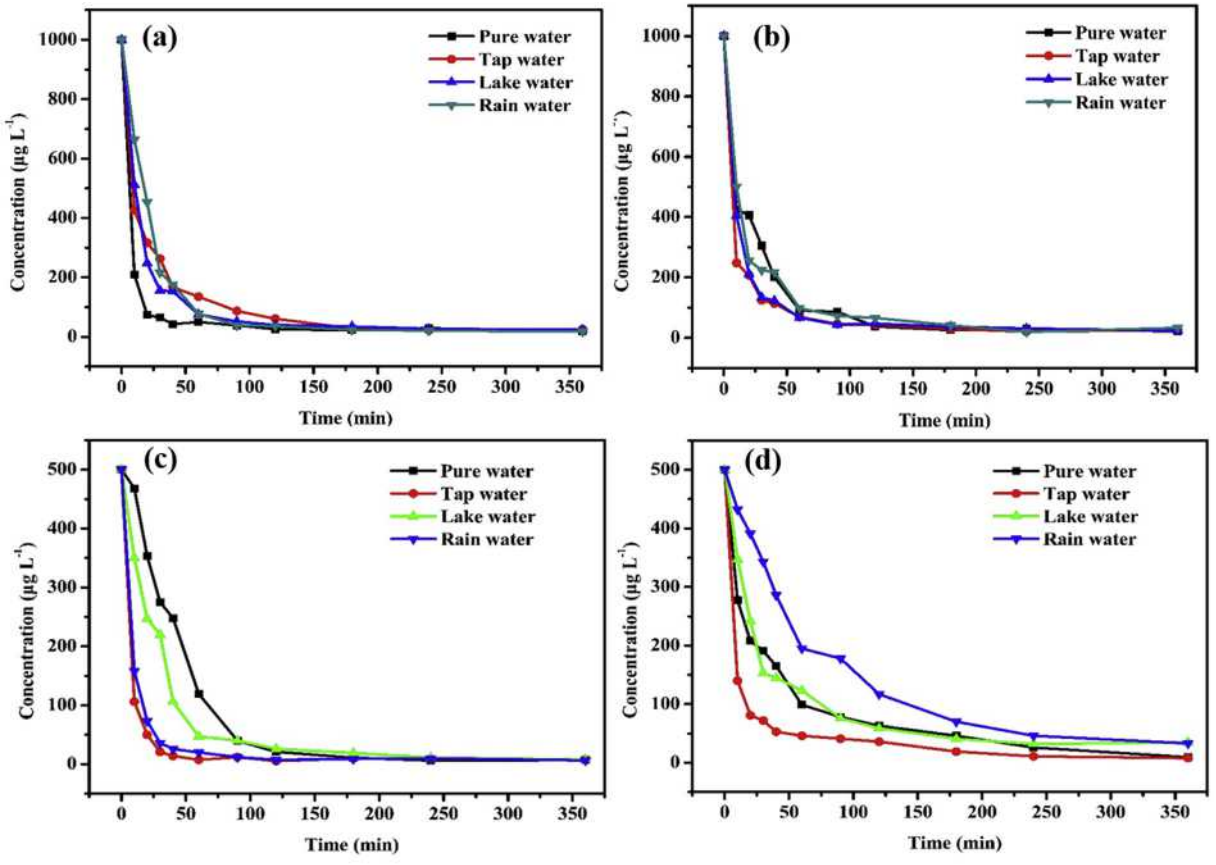

Fig. 10. The adsorption of (a) ASA, (b) ROX, (c) As(V), and (d) As(III) made up by pure, tap, lake, and rain water on the obtained **MC-2** (Initial ASA and ROX concentration: 1 mg L^{-1}; Initial As(v) and As(III) concentration: 0.5 mg L^{-1}).

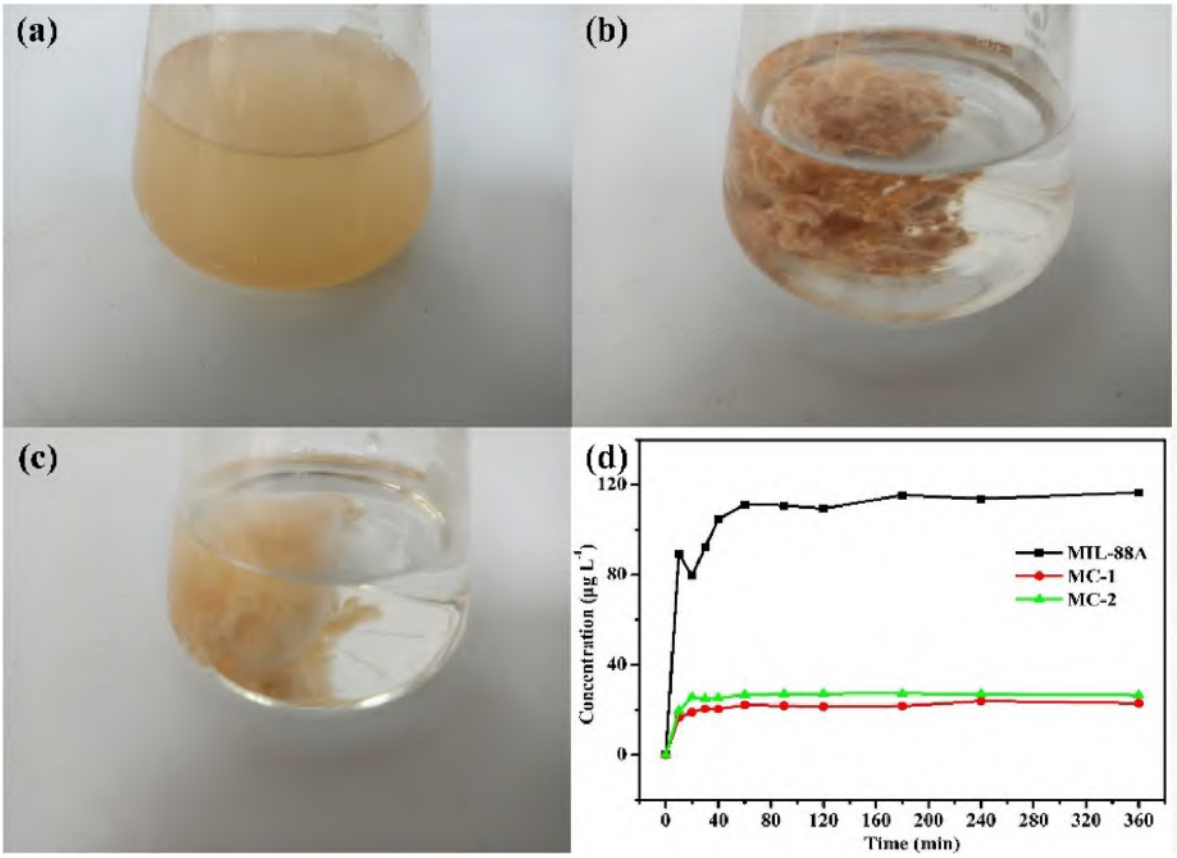

Fig. 11. The residual arsenic solution after adsorption by (a) **MIL-88A(Fe)**, (b) **MC-1**, and (c) **MC-2**; (d) The concentrations of Fe in the solution during the adsorption process.

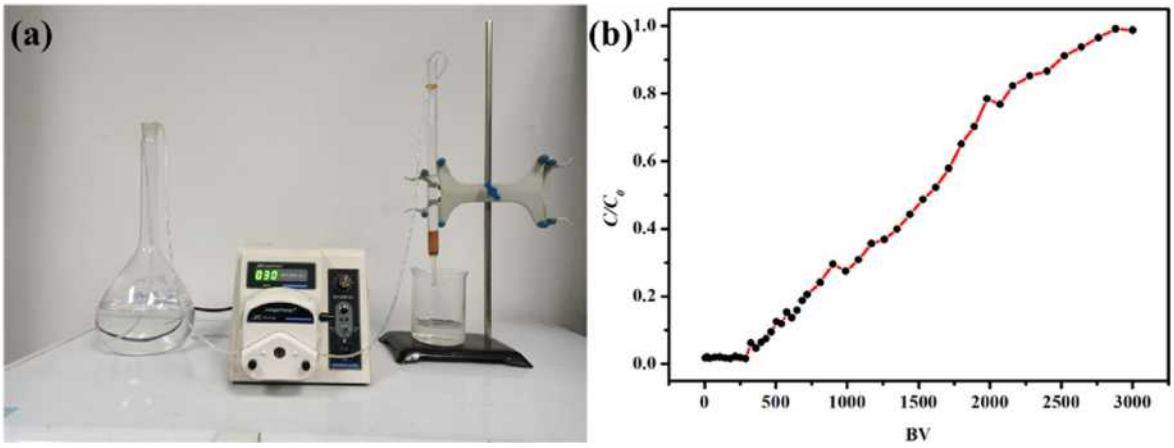

Fig. 12. (a) Equipment of fixed bed column study and (b) Breakthrough curves of ROX over **MC-1**.

solutions ranged from 252 to 432 BVs (2.52 L–4.32 L). Being compared with the pristine **MIL-88A(Fe)** particles, **MC-1** and **MC-2** displayed relatively lower adsorption capacity due to the small absolute amounts of **MIL-88A(Fe)** in the fixed-bed column. However, the adsorption performances of both **MC-1** and **MC-2** were still superior to those of the previously reported counterpart (Jun et al., 2015). This observation may be attributed to the uniform distribution and highly stable structure of **MIL-88A(Fe)**/cotton fibers, which enhances contact efficiency of **MIL-88A(Fe)** with inorganic and organic arsenic in aqueous solution. The breakthrough curve in other researches usually demonstrated an S shape and fitted well to Yoon–Nelson and Bohart–Adams model, in which the overshoot peak was presented till the adsorption saturation of the adsorbents reached (Xiong et al., 2019). However, in this study, the breakthrough curve was not perfect as theoretical models (Peng et al., 2018). The reason is that the fixed bed column experiments in this study were more closed to practical large-scale operation, which guaranteed the rapid flow of arsenic solution in order to enhance hydraulic loading rate (Ma et al., 2018). Furthermore, the leaking Fe contents in the effluents determined by ICP-

OES were maintained to zero during operation of fixed bed column experiments, implying the **MIL-88A(Fe)** in both **MC-1** and **MC-2** was stable and nearly free of Fe leaking to environment. In all, both **MC-1** and **MC-2** in fixed bed exhibited great possibility to be used in large-scale operation due to their outstanding adsorptive removal performance toward inorganic and organic arsenic pollutants from the contaminated water samples, stability and eco-environment friendly.

4. Conclusion

In this study, **MIL-88A(Fe)** with well-crystallized hexagonal microrods have been synthesized via a mild method at room temperature, which exhibited excellent adsorption abilities toward inorganic and organic arsenic pollutants. The maximum adsorption capacities of **MIL-88A(Fe)** towards As(III), As(V), ROX and ASA was 126.5, 164.0, 261.4 and 427.5 mg g^{-1}, respectively, which was higher than most counterpart adsorbents. The adsorption kinetics and adsorption isotherm of various arsenic species on **MIL-88A(Fe)** can be described by the pseudo-second-order kinetic model and Langmuir isotherm model, respectively. The outstanding adsorption performances of **MIL-88A(Fe)** toward different arsenic pollutants can be assigned to the coordinative interactions of As—O—Fe between arsenic pollutants and **MIL-88A(Fe)**. To achieve good recyclability and facile separation, **MIL-88A(Fe)** was decorated on cotton fibers via both post synthetic method and in-situ growth method to obtain **MC-1** and **MC-2** composites, which demonstrated identically outstanding removal efficiencies towards inorganic and organic arsenic pollutants in simulated water samples. The fixed-bed column experiments further demonstrated that **MC-1** and **MC-2** could be potentially used for large-scale removal of arsenic pollutants. This work provided us possibility to weave the cotton fibers decorated with **MIL-88A(Fe)** into threads and even cloth or web, which was used to capture the arsenic pollutants from the real water system.

Credit author statement

Da Pang: Data curation, Investigation, Visualization, Writing-Original draft preparation., Wang Chong-Chen: Conceptualization, Funding acquisition, Supervision, Project administration, Writing - review & editing, Wang Peng: Resources, Visualization, Instrumenta, Wen Liu: Methodology, Software, Fu Huifen: Validation, Software, Zhao Chen: Software, Instrumental.

Acknowledgements

This work was supported by National Natural Science Foundation of China (51878023), Beijing Municipal Natural Science Foundation, Great Wall Scholars Training Program Project of Beijing Municipality Universities (CIT&TCD20180323), and Beijing Talent Project (2019A22).

Appendix A. Supplementary data

Supplementary data to this article can be found online at https://doi.org/10.1016/j.chemosphere.2020.126829.

Declaration of interests

The authors declare that they have no known competing financial interests or personal relationships that could have appeared to influence the work reported in this paper.

References

Abdelhameed, R.M., Rehan, M., Emam, H.E., 2018. Figuration of Zr-based MOF@cotton fabric composite for potential kidney application. Carbohydr. Polym. 195, 460–467.
Ahmad, S.Z.N., Wan Salleh, W.N., Ismail, A.F., Yusof, N., Mohd Yusop, M.Z., Aziz, F., 2020. Adsorptive removal of heavy metal ions using graphene-based nanomaterials: toxicity, roles of functional groups and mechanisms. Chemosphere 248, 126008.
Cai, J., Wang, X., Zhou, Y., Jiang, L., Wang, C., 2016. Selective adsorption of arsenate and reversible structure transformation of mesoporous metal-organic framework MIL-100(Fe). Phys. Chem. Chem. Phys. 18, 10864–10867.
Chen, B., Zhu, Z., Guo, Y., Qiu, Y., Zhao, J., 2013. Facile synthesis of mesoporous Ce-Fe bimetal oxide and its enhanced adsorption of arsenate from aqueous solutions. J. Colloid Interface Sci. 398, 142–151.
Chen, W., Parette, R., Zou, J., Cannon, F.S., Dempsey, B.A., 2007. Arsenic removal by iron-modified activated carbon. Water Res. 41, 1851–1858.
Choong, T.S.Y., Chuah, T.G., Robiah, Y., Gregory Koay, F.L., Azni, I., 2007. Arsenic toxicity, health hazards and removal techniques from water: an overview. Desalination 217, 139–166.
Deng, S., zhang, G., Chen, S., Xue, Y., Du, Z., Wang, P., 2016. Rapid and effective preparation of a HPEI modified biosorbent based on cellulose fiber with a microwave irradiation method for enhanced arsenic removal in water. J. Mater. Chem. A. 4, 15851–15860.
Ding, K., Wang, W., Yu, D., Wang, W., Gao, P., Liu, B., 2018. Facile formation of flexible Ag/AgCl/polydopamine/cotton fabric composite photocatalysts as an efficient visible-light photocatalysts. Appl. Surf. Sci. 454, 101–111.
Du, X.-D., Wang, C.-C., Liu, J.-G., Zhao, X.-D., Zhong, J., Li, Y.-X., Li, J., Wang, P., 2017. Extensive and selective adsorption of ZIF-67 towards organic dyes: performance and mechanism. J. Colloid Interface Sci. 506, 437–441.
Du, X.-D., Yi, X.-H., Wang, P., Zheng, W., Deng, J., Wang, C.-C., 2019. Robust photocatalytic reduction of Cr(VI) on UiO-66-NH_2(Zr/Hf) metal-organic framework membrane under sunlight irradiation. Chem. Eng. J. 356, 393–399.
Farha, O.K., Özgür Yazaydın, A., Eryazici, I., Malliakas, C.D., Hauser, B.G., Kanatzidis, M.G., Nguyen, S.T., Snurr, R.Q., Hupp, J.T., 2010. De novo synthesis of a metal-organic framework material featuring ultrahigh surface area and gas storage capacities. Nat. Chem. 2, 944–948.
Fiamingo, A., Campana-Filho, S.P., 2016. Structure, morphology and properties of genipin-crosslinked carboxymethylchitosan porous membranes. Carbohydr. Polym. 143, 155–163.
Folens, K., Leus, K., Nicomel, N.R., Meledina, M., Turner, S., Van Tendeloo, G., Laing, G.D., Van Der Voort, P., 2016. Fe_3O_4@MIL-101 - a selective and regenerable adsorbent for the removal of as species from water. Eur. J. Inorg. Chem. 4395–4401, 2016.
Fu, H., Song, X.-X., Wu, L., Zhao, C., Wang, P., Wang, C.-C., 2019. Room-temperature preparation of MIL-88A as a visible-light-driven photocatalyst for degradation of rhodamine B and bisphenol A. Mater. Res. Bull. 112, 241–247.
Fu, H., Song, X.-X., Wu, L., Zhao, C., Wang, P., Wang, C.-C., 2020. Room-temperature preparation of MIL-88A as a heterogeneous photo-Fenton catalyst for degradation of rhodamine B and bisphenol a under visible light. Mater. Res. Bull. 125, 110806.
Gargoubi, S., Tolouei, R., Chevallier, P., Levesque, L., Ladhari, N., Boudokhane, C., Mantovani, D., 2016. Enhancing the functionality of cotton fabric by physical and chemical pre-treatments: a comparative study. Carbohydr. Polym. 147, 28–36.
Gholizadeh Khasevani, S., Gholami, M.R., 2018. Engineering a highly dispersed core@shell structure for efficient photocatalysis: a case study of ternary novel BiOI@MIL-88A(Fe)@g-C_3N_4 nanocomposite. Mater. Res. Bull. 106, 93–102.
Guan, X., Du, J., Meng, X., Sun, Y., Sun, B., Hu, Q., 2012. Application of titanium dioxide in arsenic removal from water: a review. J. Hazard Mater. 215–216, 1–16.
He, X., Deng, F., Shen, T., Yang, L., Chen, D., Luo, J., Luo, X., Min, X., Wang, F., 2019. Exceptional adsorption of arsenic by zirconium metal-organic frameworks: Engineering exploration and mechanism insight. J. Colloid Interface Sci. 539, 223–234.
Hou, S., Wu, Y.-n., Feng, L., Chen, W., Wang, Y., Morlay, C., Li, F., 2018. Green synthesis and evaluation of an iron-based metal-organic framework MIL-88B for efficient decontamination of arsenate from water. Dalton Trans. 47, 2222–2231.
Hu, Q., Liu, Y., Gu, X., Zhao, Y., 2017. Adsorption behavior and mechanism of different arsenic species on mesoporous $MnFe_2O_4$ magnetic nanoparticles. Chemosphere 181, 328–336.
Huang, W., Jing, C., Zhang, X., Tang, M., Tang, L., Wu, M., Liu, N., 2018. Integration of plasmonic effect into spindle-shaped MIL-88A(Fe): steering charge flow for enhanced visible-light photocatalytic degradation of ibuprofen. Chem. Eng. J. 349, 603–612.
Hughes, M.F., Beck, B.D., Chen, Y., Lewis, A.S., Thomas, D.J., 2011. Arsenic exposure and toxicology: a historical perspective. Technol. Sci. 123, 305–332.
Huo, J.-B., Xu, L., Yang, J.-C.E., Cui, H.-J., Yuan, B., Fu, M.-L., 2018. Magnetic responsive Fe_3O_4-ZIF-8 core-shell composites for efficient removal of As(III) from water. Colloids Surf., A 539, 59–68.
Jian, M., Liu, B., Zhang, G., Liu, R., Zhang, X., 2015. Adsorptive removal of arsenic from aqueous solution by zeolitic imidazolate framework-8 (ZIF-8) nanoparticles. Colloids Surf., A 465, 67–76.
Joshi, T.P., Zhang, G., Jefferson, W.A., Perfilev, A.V., Liu, R., Liu, H., Qu, J., 2017. Adsorption of aromatic organoarsenic compounds by ferric and manganese

binary oxide and description of the associated mechanism. Chem. Eng. J. 309, 577–587.
Jun, J.W., Tong, M., Jung, B.K., Hasan, Z., Zhong, C., Jhung, S.H., 2015. Effect of central metal ions of analogous metal-organic frameworks on adsorption of organo-arsenic compounds from water: plausible mechanism of adsorption and water purification. Chem. Eur J. 21, 347–354.
Jung, B.K., Jun, J.W., Hasan, Z., Jhung, S.H., 2015. Adsorptive removal of p-arsanilic acid from water using mesoporous zeolitic imidazolate framework-8. Chem. Eng. J. 267, 9–15.
Kang, D., Yu, X., Tong, S., Ge, M., Zuo, J., Cao, C., Song, W., 2013. Performance and mechanism of Mg/Fe layered double hydroxides for fluoride and arsenate removal from aqueous solution. Chem. Eng. J. 228, 731–740.
Li, B., Zhu, X., Hu, K., Li, Y., Feng, J., Shi, J., Gu, J., 2016. Defect creation in metal-organic frameworks for rapid and controllable decontamination of roxarsone from aqueous solution. J. Hazard Mater. 302, 57–64.
Li, J., Wang, H., Yuan, X., Zhang, J., Chew, J.W., 2020. Metal-organic framework membranes for wastewater treatment and water regeneration. Coord. Chem. Rev. 404, 213116.
Li, L., Zhao, J., Sun, Y., Yu, F., Ma, J., 2019. Ionically cross-linked sodium alginate/κ-carrageenan double-network gel beads with low-swelling, enhanced mechanical properties, and excellent adsorption performance. Chem. Eng. J. 372, 1091–1103.
Li, X., Pi, Y., Wu, L., Xia, Q., Wu, J., Li, Z., Xiao, J., 2017. Facilitation of the visible light-induced Fenton-like excitation of H_2O_2 via heterojunction of g-C_3N_4/NH_2-Iron terephthalate metal-organic framework for MB degradation. Appl. Catal. B Environ. 202, 653–663.
Liang, R., Jing, F., Shen, L., Qin, N., Wu, L., 2015a. MIL-53(Fe) as a highly efficient bifunctional photocatalyst for the simultaneous reduction of Cr(VI) and oxidation of dyes. J. Hazard Mater. 287, 364–372.
Liang, R., Shen, L., Jing, F., Qin, N., Wu, L., 2015b. Preparation of MIL-53(Fe)-Reduced graphene oxide nanocomposites by a simple self-assembly strategy for increasing interfacial contact: efficient visible-light photocatalysts. ACS Appl. Mater. Interfaces 7, 9507–9515.
Liao, X., Wang, F., Wang, F., Cai, Y., Yao, Y., Teng, B.-T., Hao, Q., Lu, S., 2019. Synthesis of (100) surface oriented MIL-88A-Fe with rod-like structure and its enhanced fenton-like performance for phenol removal. Appl. Catal. B Environ. 259, 118064.
Liu, A., Wang, C.-C., Wang, C.-z., Fu, H.-f., Peng, W., Cao, Y.-L., Chu, H.-Y., Du, A.-F., 2018a. Selective adsorption activities toward organic dyes and antibacterial performance of silver-based coordination polymers. J. Colloid Interface Sci. 512, 730–739.
Liu, B., Jian, M., Liu, R., Yao, J., Zhang, X., 2015a. Highly efficient removal of arsenic(III) from aqueous solution by zeolitic imidazolate frameworks with different morphology. Colloids Surf., A 481, 358–366.
Liu, K., Zhang, S., Hu, X., Zhang, K., Roy, A., Yu, G., 2015b. Understanding the adsorption of PFOA on MIL-101(Cr)-Based anionic-exchange metal-organic frameworks: comparing DFT calculations with aqueous sorption experiments. Environ. Sci. Technol. 49, 8657–8665.
Liu, N., Huang, W., Zhang, X., Tang, L., Wang, L., Wang, Y., Wu, M., 2018b. Ultrathin graphene oxide encapsulated in uniform MIL-88A(Fe) for enhanced visible light-driven photodegradation of RhB. Appl. Catal. B Environ. 221, 119–128.
Liu, X., Zhang, W., Hu, Y., Hu, E., Xie, X., Wang, L., Cheng, H., 2015c. Arsenic pollution of agricultural soils by concentrated animal feeding operations (CAFOs). Chemosphere 119, 273–281.
Lv, H., Ji, G., Liu, W., Zhang, H., Du, Y., 2015. Achieving hierarchical hollow carbon@Fe@Fe_3O_4 nanospheres with superior microwave absorption properties and lightweight features. J. Mater. Chem. C. 3, 10232–10241.
Lv, J., Zhou, Q., Liu, G., Gao, D., Wang, C., 2014. Preparation and properties of polyester fabrics grafted with O-carboxymethyl chitosan. Carbohydr. Polym. 113, 344–352.
Lv, Y., Zhang, R., Zeng, S., Liu, K., Huang, S., Liu, Y., Xu, P., Lin, C., Cheng, Y., Liu, M., 2018. Removal of p-arsanilic acid by an amino-functionalized indium-based metal–organic framework: adsorption behavior and synergetic mechanism. Chem. Eng. J. 339, 359–368.
Ma, J., Liu, Y., Ali, O., Wei, Y., Zhang, S., Zhang, Y., Cai, T., Liu, C., Luo, S., 2018. Fast adsorption of heavy metal ions by waste cotton fabrics based double network hydrogel and influencing factors insight. J. Hazard Mater. 344, 1034–1042.
Ma, J., Zhuang, Y., Yu, F., 2015. Equilibrium, kinetic and thermodynamic adsorption studies of organic pollutants from aqueous solution onto CNT/C@Fe/chitosan composites. New J. Chem. 39, 9299–9305.
Martinson, C.A., Reddy, K.J., 2009. Adsorption of arsenic(III) and arsenic(V) by cupric oxide nanoparticles. J. Colloid Interface Sci. 336, 406–411.
McKinlay, A.C., Eubank, J.F., Wuttke, S., Xiao, B., Wheatley, P.S., Bazin, P., Lavalley, J.C., Daturi, M., Vimont, A., De Weireld, G., Horcajada, P., Serre, C., Morris, R.E., 2013. Nitric oxide adsorption and delivery in flexible MIL-88(Fe) metal–organic frameworks. Chem. Mater. 25, 1592–1599.
Moghimi, N., Mohapatra, M., Leung, K.T., 2015. Bimetallic nanoparticles for arsenic detection. Anal. Chem. 87, 5546–5552.
Muñiz, G., Fierro, V., Celzard, A., Furdin, G., Gonzalez-Sánchez, G., Ballinas, M.L., 2009. Synthesis, characterization and performance in arsenic removal of iron-doped activated carbons prepared by impregnation with Fe(III) and Fe(II). J. Hazard Mater. 165, 893–902.
Naebe, M., Li, Q., Onur, A., Denning, R., 2016. Investigation of chitosan adsorption onto cotton fabric with atmospheric helium/oxygen plasma pre-treatment. Cellulose 23, 2129–2142.
Nasir, A.M., Md Nordin, N.A.H., Goh, P.S., Ismail, A.F., 2018. Application of two-dimensional leaf-shaped zeolitic imidazolate framework (2D ZIF-L) as arsenite adsorbent: kinetic, isotherm and mechanism. J. Mol. Liq. 250, 269–277.
Peng, Y., Huang, H., Zhang, Y., Kang, C., Chen, S., Song, L., Liu, D., Zhong, C., 2018. A versatile MOF-based trap for heavy metal ion capture and dispersion. Nat. Commun. 9, 187.
Poon, L., Younus, S., Wilson, L.D., 2014. Adsorption study of an organo-arsenical with chitosan-based sorbents. J. Colloid Interface Sci. 420, 136–144.
Ramsahye, N.A., Trung, T.K., Scott, L., Nouar, F., Devic, T., Horcajada, P., Magnier, E., David, O., Serre, C., Trens, P., 2013. Impact of the flexible character of MIL-88 iron(III) dicarboxylates on the adsorption of n-alkanes. Chem. Mater. 25, 479–488.
Sarker, M., Song, J.Y., Jhung, S.H., 2017. Adsorption of organic arsenic acids from water over functionalized metal-organic frameworks. J. Hazard Mater. 335, 162–169.
Sierra-Alvarez, R., Cortinas, I., Field, J.A., 2010. Methanogenic inhibition by roxarsone (4-hydroxy-3-nitrophenylarsonic acid) and related aromatic arsenic compounds. J. Hazard Mater. 175, 352–358.
Smedley, P.L., Kinniburgh, D.G., 2002. A review of the source, behaviour and distribution of arsenic in natural waters. Appl. Geochem. 17, 517–568.
Smith, A.H., Lopipero, P.A., Bates, M.N., Steinmaus, C.M., 2002. Arsenic epidemiology and drinking water standards. Science 296, 2145–2146.
Song, P., Yang, Z., Zeng, G., Yang, X., Xu, H., Wang, L., Xu, R., Xiong, W., Ahmad, K., 2017. Electrocoagulation treatment of arsenic in wastewaters: a comprehensive review. Chem. Eng. J. 317, 707–725.
Song, X.-X., Fu, H., Wang, P., Li, H.-Y., Zhang, Y.-Q., Wang, C.-C., 2018. The selectively fluorescent sensing detection and adsorptive removal of Pb^{2+} with a stable [delta-Mo_8O_{26}]-based hybrid. J. Colloid Interface Sci. 532, 598–604.
Sui, J., Wang, L., Zhao, W., Hao, J., 2016. Iron-naphthalenedicarboxylic acid gels and their high efficiency in removing arsenic(V). Chem. Commun. 52, 6993–6996.
Tian, C., Zhao, J., Ou, X., Wan, J., Cai, Y., Lin, Z., Dang, Z., Xing, B., 2018. Enhanced adsorption of p-arsanilic acid from water by amine-modified UiO-67 as examined using extended X-ray absorption fine structure, X-ray photoelectron spectroscopy, and density functional theory calculations. Environ. Sci. Technol. 52, 3466–3475.
Valizadeh, B., Nguyen, T.N., Smit, B., Stylianou, K.C., 2018. Porous metal-organic Framework@Polymer beads for iodine capture and recovery using a gas-sparged column. Adv. Funct. Mater. 28, 1801596.
Vu, T.A., Le, G.H., Dao, C.D., Dang, L.Q., Nguyen, K.T., Nguyen, Q.K., Dang, P.T., Tran, H.T.K., Duong, Q.T., Nguyen, T.V., Lee, G.D., 2015. Arsenic removal from aqueous solutions by adsorption using novel MIL-53(Fe) as a highly efficient adsorbent. RSC Adv. 5, 5261–5268.
Wang, C.-C., Li, J.-R., Lv, X.-L., Zhang, Y.-Q., Guo, G., 2014. Photocatalytic organic pollutants degradation in metal–organic frameworks. Energy Environ. Sci. 7, 2831–2867.
Wang, C.-C., Yi, X.-H., Wang, P., 2019a. Powerful combination of MOFs and C_3N_4 for enhanced photocatalytic performance. Appl. Catal. B Environ. 247, 24–48.
Wang, C., Luan, J., Wu, C., 2019b. Metal-organic frameworks for aquatic arsenic removal. Water Res. 158, 370–382.
Wang, C.Y., Fu, H., Wang, P., Wang, C.C., 2019c. Highly sensitive and selective detect of p -arsanilic acid with a new water-stable europium metal–organic framework. Appl. Organomet. Chem. 33, 5021–5029.
Wang, L., Cheng, H., 2015. Birnessite (delta-MnO_2) mediated degradation of organoarsenic feed additive p-arsanilic acid. Environ. Sci. Technol. 49, 3473–3481.
Wang, W., Li, M., Zeng, Q., 2015. Adsorption of chromium (VI) by strong alkaline anion exchange fiber in a fixed-bed column: experiments and models fitting and evaluating. Separ. Purif. Technol. 149, 16–23.
Wang, Z., Zhang, J., Wu, Q., Han, X., Zhang, M., Liu, W., Yao, X., Feng, J., Dong, S., Sun, J., 2020. Magnetic supramolecular polymer: ultrahigh and highly selective Pb(II) capture from aqueous solution and battery wastewater. Chemosphere 248, 126042.
Wu, Y.-n., Zhou, M., Zhang, B., Wu, B., Li, J., Qiao, J., Guan, X., Li, F., 2014. Amino acid assisted templating synthesis of hierarchical zeolitic imidazolate framework-8 for efficient arsenate removal. Nanoscale 6, 1105–1112.
Xia, Q., Wang, H., Huang, B., Yuan, X., Zhang, J., Zhang, J., Jiang, L., Xiong, T., Zeng, G., 2019. State-of-the-Art advances and challenges of iron-based metal organic frameworks from attractive features, synthesis to multifunctional applications. Small 15, 1803088.
Xiao, L., Xiong, Y., Tian, S., He, C., Su, Q., Wen, Z., 2015. One-dimensional coordination supramolecular polymer $[Cu(bipy)(SO_4)]_n$ as an adsorbent for adsorption and kinetic separation of anionic dyes. Chem. Eng. J. 265, 157–163.
Xie, D., Ma, Y., Gu, Y., Zhou, H., Zhang, H., Wang, G., Zhang, Y., Zhao, H., 2017. Bifunctional NH_2-MIL-88(Fe) metal–organic framework nanooctahedra for highly sensitive detection and efficient removal of arsenate in aqueous media. J. Mater. Chem. A. 5, 23794–23804.
Xiong, W.-l., Zhang, J., Yu, J.-x., Chi, R.-a., 2019. Competitive adsorption behavior and mechanism for Pb2+ selective removal from aqueous solution on phosphoric acid modified sugarcane bagasse fixed-bed column. Process. Saf. Environ. 124, 75–83.
Xu, Q., Xie, L., Diao, H., Li, F., Zhang, Y., Fu, F., Liu, X., 2017. Antibacterial cotton fabric with enhanced durability prepared using silver nanoparticles and carboxymethyl chitosan. Carbohydr. Polym. 177, 187–193.
Xu, W.-T., Ma, L., Ke, F., Peng, F.-M., Xu, G.-S., Shen, Y.-H., Zhu, J.-F., Qiu, L.-G., Yuan, Y.-P., 2014. Metal-organic frameworks MIL-88A hexagonal microrods as a new photocatalyst for efficient decolorization of methylene blue dye. Dalton

Trans. 43, 3792–3798.
Xu, X.-Y., Chu, C., Fu, H., Du, X.-D., Wang, P., Zheng, W., Wang, C.-C., 2018. Light-responsive UiO-66-NH_2/Ag_3PO_4 MOF-nanoparticle composites for the capture and release of sulfamethoxazole. Chem. Eng. J. 350, 436–444.
Yang, D., Velamakanni, A., Bozoklu, G., Park, S., Stoller, M., Piner, R.D., Stankovich, S., Jung, I., Field, D.A., Ventrice, C.A., Ruoff, R.S., 2009. Chemical analysis of graphene oxide films after heat and chemical treatments by X-ray photoelectron and Micro-Raman spectroscopy. Carbon 47, 145–152.
Yi, X.-H., Ma, S.-Q., Du, X.-D., Zhao, C., Fu, H., Wang, P., Wang, C.-C., 2019. The facile fabrication of 2D/3D Z-scheme g-C_3N_4/UiO-66 heterojunction with enhanced photocatalytic Cr(VI) reduction performance under white light. Chem. Eng. J. 375, 121944.
You, Y., Liang, Y., Peng, S., Lan, S., Lu, G., Feng, X., Shi, Z., 2020. Modeling coupled kinetics of arsenic adsorption/desorption and oxidation in ferrihydrite-Mn(II)/manganese (oxyhydr)oxides systems. Chemosphere 244, 125517.
Yu, C., Gou, L., Zhou, X., Bao, N., Gu, H., 2011. Chitosan–Fe_3O_4 nanocomposite based electrochemical sensors for the determination of bisphenol A. Electrochim. Acta 56, 9056–9063.
Yu, F., Sun, Y., Yang, M., Ma, J., 2019. Adsorption mechanism and effect of moisture contents on ciprofloxacin removal by three-dimensional porous graphene hydrogel. J. Hazard Mater. 374, 195–202.
Zhang, T., Wang, J., Zhang, W., Yang, C., Zhang, L., Zhu, W., Sun, J., Li, G., Li, T., Wang, J., 2019. Amorphous Fe/Mn bimetal-organic frameworks: outer and inner structural design for efficient arsenic(III) removal. J. Mater. Chem. A. 7, 2845–2854.
Zhao, C., Wang, C.-C., Li, J.-Q., Wang, P., Ou, J.-Q., Cui, J.-R., 2018. Interactions between copper(II) and DOM in the urban stormwater runoff: modeling and characterizations. Environ. Technol. 39, 120–129.
Zietzschmann, F., Stutzer, C., Jekel, M., 2016. Granular activated carbon adsorption of organic micro-pollutants in drinking water and treated wastewater-aligning breakthrough curves and capacities. Water Res. 92, 180–187.